Chalcogenide Letters

Tech Science Press

http://doi.org/10.32604/cl.2026.085815

ARTICLE

Synthesis, Crystal Structure, Optical, and Thermal Properties of a Novel Quaternary Selenide $EuErAgSe_3$

Navruzbek Habibullayev[1,*], Ilya Yurev[1,2], Maxim Molokeev[1,3,4], Aleksandr Aleksandrovsky[3,5], Olga Trofimova[1], Nikita Shulaev[1], Svetlana Volkova[1] and Oleg Andreev[1,6]

[1]University of Tyumen, Volodarskogo St., 6, Tyumen, Russia
[2]Kurgan State University, Sovetskaya St., 63, Building 4, Kurgan, Russia
[3]Kirensky Institute of Physics, Akademgorodok St., 50, Building 38, Krasnoyarsk, Russia
[4]Far Eastern State Transport University, Seryshev St., 47, Khabarovsk, Russia
[5]Siberian Federal University, Svobodny Pr., 79, Krasnoyarsk, Russia
[6]Institute of Solid State Chemistry of the Ural Branch of the Russian Academy of Sciences, Pervomaiskaya St., 91, Ekaterinburg, Russia
*Corresponding Author: Navruzbek Habibullayev. Email: habibullayev_navruzbek@mail.ru

Received: 19 May 2026; Accepted: 29 June 2026; Published: 07 August 2026

ABSTRACT: A novel quaternary selenide, $EuErAgSe_3$, has been synthesized for the first time. The phase forms upon annealing in the 1120–1800 K range and retains its crystal structure upon cooling to ambient conditions. The phase was prepared by the ampoule method from EuSe and $AgErSe_2$ powders, followed by annealing at 1270 ± 10 K for up to 300 h. Powder X-ray diffraction revealed that $EuErAgSe_3$ crystallizes in the $AgBiS_2$ structure type (space group *Fm*-3*m*) with the lattice parameter a = 5.95322(14) Å. The microhardness of the phase is 340 ± 15 HV. The optical band gap for direct transitions is 1.78 eV, and for indirect transitions, it is 1.36 eV. The phase begins to form in the temperature range 1120–1170 K, likely due to diffusion processes, and melts incongruently at 1830 ± 30 K. The formation of $EuLnAgSe_3$ phases was predicted for Ln = Gd–Lu, Y and confirmed experimentally for Gd, with a = 5.9906(4) Å, and for Yb, with a = 5.9312(5) Å. In the $EuLnAgSe_3$ series, the unit cell parameter decreases linearly with the ionic radius of Ln^{3+}.

KEYWORDS: Quaternary rare-earth selenides; cation-disordered cubic structure; optical band gap; incongruent melting; artificial intelligence

1 Introduction

Quaternary rare-earth chalcogenides with the general formula $A^{2+}RE^{3+}Ag^{+}X_3^{2-}$ (A = Sr, Ba, Eu; Ln = rare-earth metals (RE); X = S, Se, Te) are promising optical and thermoelectric materials [1–3]. Quaternary chalcogenides crystallizing in the $AgBiS_2$ structure type are few in number and are regarded as promising semiconducting materials [4], while the presence of Er^{3+} ions in the lattice enables efficient upconversion photoluminescence and makes such matrices suitable for optical temperature sensors [5]. For $AgLnSe_2$ selenides, the cubic NaCl-type structure (space group F*m-3m*) is observed only for high-temperature modifications of the compounds with heavy lanthanides (Ln = Gd–Lu and Y), whereas when the synthesis temperature is lowered the same elements form orthorhombic or monoclinic superstructures [6,7]. Light lanthanides (La–Nd, Sm) in the whole studied range of conditions crystallize exclusively in layered monoclinic or orthorhombic polytypes that belong to the α-$AgLaS_2$ structure family. For the Eu^{2+} cation ($4f^7$ $5d^0$ $6s^0$, rEu^{2+} (CN = 6) = 1.17 Å), six quaternary sulfides: $EuREAgS_3$ (RE = Gd, Tb, Dy, Ho, Tm, Yb), have been obtained [4,8]. $EuTmAgS_3$ and $EuYbAgS_3$ crystallize in

the trigonal system, space group *R-3m*, NiO structure type. Compounds $EuREAgS_3$ (RE = Gd, Dy, Ho) exist as two polymorphic modifications; the low-temperature modifications α-$EuREAgS_3$ crystallize in the monoclinic system, space group *C*2/*m*, $BaErAgS_3$ structure type. The high-temperature modifications β-$EuREAgS_3$ belong to the space group *Fm*-3*m*, CT $AgBiS_2$ structure type, with unit cell parameters a = 5.739(2) Å, a = 5.697(2) and a = 5.678 Å, respectively. In the series of compounds with a cubic structure, a linear decrease in the average bond lengths d(Eu/RE/Ag–S) is observed with decreasing RE^{3+} ionic radius, which confirms the stoichiometry of the compositions.

No reports on the synthesis, structure, thermal stability, or properties of possible compounds of the $EuLnAgSe_3$ series have been reported in the literature. Erbium (Er $4f^{12}6s^2$) is a typical rare-earth element of the yttrium subgroup and exhibits an oxidation state of +3. The synthesis and study of phases formed by erbium makes it possible to predict phase compositions for RE elements of the yttrium subgroup on the basis of the tetrad effect [9–11].

The composition of the quaternary compounds (0.5 Ag_2Se + 0.5 Ln_2Se_3 + EuSe (Ln = Sm − Lu)) lies in the Ag_2Se–$AgLnSe_2$–EuSe system. The low-temperature modification α-Ag_2Se transforms at 407 K into the β-Ag_2Se modification [12], which melts at 1170 K [13]. The melting point of $AgErSe_2$ is not reported in the literature; however, based on the available data for the related compounds $AgHoSe_2$ and $AgDyS_2$, it is estimated to lie in the range 1500–1600 K. The phase transition temperature of $AgHoSe_2$ is 1050 K [7], while for $AgDyS_2$ the phase transition temperature is 1280 K and the melting point is 1830 K [14]. EuSe melts at 2488 K [15]. According to [16], the $EuSe_2$ phase crystallizes in the tetragonal system, space group *I*4/*mcm*, CT $CuAl_2$ structure type, and begins to decompose at 842 K with the formation of EuSe.

The formation of new phases or solid solutions between isostructural phases can be examined using the Hume-Rothery rule. The Hume-Rothery rule considers the conditions for the formation of solid solutions and new compounds [17]. The formation of solid solutions requires similarity of crystal lattices, a difference in atomic radii of no more than 15%, and the same valence of the elements. An electronegativity difference exceeding 0.4–0.5 favors the formation of a new phase.

In this work, we report the synthesis of $EuErAgSe_3$, its crystallochemical characteristics, optical band gap, thermal properties, and a prediction of the formation of $EuLnAgSe_3$ phases for yttrium-subgroup rare-earth elements.

2 Materials and Methods

2.1 Synthesis

The rare-earth metals (99.99 at.% La, Nd, Sm, Gd, Er, Yb) were used in the form of pieces, europium oxalate powder (99.98 wt.% $EuC_2O_4{\cdot}nH_2O$) (Toplus, Ltd., Guangzhou, China), silver (99.99 at.% Ag) as an ingot, and selenium granules (99.998 at.% Se) (JSC Khimreaktiv, Yekaterinburg, Russia). Hydrogen gas (99.999%) was obtained by electrolysis of deionized water in a generator (Spektr LLC, Dzerzhinsk, Russia). Crucibles were made of MG-1 grade graphite.

The $EuErAgSe_3$ sample was synthesized by the ampoule method from EuSe and $AgErSe_2$. EuSe was obtained by the action of an H_2Se flow on europium oxalate powder at temperatures of 1120–1220 ± 10 K [18]. The product was a dark brown powder of phase-pure EuSe, which adopted the NaCl-type structure (*Fm-3m*, a = 6.1676 Å) [19].

$AgErSe_2$ was synthesized from the elemental substances. Weighed portions of the substances (±0.0001 g) were placed in a graphite crucible inside a quartz ampoule. The ampoules were evacuated to 0.2 Pa and sealed. The ampoule with the substance was heated to 1170 ± 10 K at a rate of 5 K/h and then held at 1170 ± 10 K for 100 h. The sintered cake obtained in the crucible was annealed at 1500–1520 ± 20 K for 20 min by heating

the crucible by induction with high-frequency currents. Subsequently, the ampoule containing the resulting cylindrical sample was annealed in a muffle furnace at 1170 ± 10 K for up to 300 h. A phase-pure $AgErSe_2$ sample was obtained. It crystallizes in the orthorhombic structure (space group $P2_12_12_1$) with unit cell parameters a = 4.1527 Å, b = 6.8041 Å, c = 13.6201 Å [7].

To synthesize $EuErAgSe_3$ in an amount of 5 g, weighed portions of EuSe and $AgErSe_2$ were ground together in an agate mortar and placed in a graphite crucible inside a quartz ampoule, which was evacuated and sealed. In a high-frequency current setup, the crucible was heated to 1620 ± 20 K and held for 20 min. Dense, partially melted sinters containing more than 90 mol.% $EuErAgSe_3$ were obtained. Subsequently, the ampoule with the sample was annealed in a muffle furnace at 1270 ± 10 K for up to 500 h. The resulting sample contained 98 ± 2 mol.% $EuErAgSe_3$. Afterwards, the sample was divided into two parts: one part was left for physicochemical study, the second part was annealed at 720 ± 10 K in a closed evacuated ampoule for up to 500 h.

Synthesis of $EuLnAgSe_3$ samples (Ln = La, Nd, Sm, Gd, Yb) was carried out by the ampoule method from the binary metal selenides Ln_2Se_3, EuSe and $Ag_{1.9}Se$ [18]. The $Ag_{1.9}Se$ precursor was prepared in an evacuated and sealed quartz ampoule, which was heated to 1270 ± 10 K at a rate of 100 K/h and subsequently cooled in air. A polycrystalline silver-colored sample containing 100 mol% $Ag_{1.9}Se$ was obtained; its unit cell parameters are a = 4.1527 Å, b = 6.8041 Å, c = 13.6201 Å, space group $P2_12_12_1$ [20]. Ln_2Se_3 compounds (Ln = La, Nd, Sm, Gd, Tb, Yb) were also synthesized by the ampoule method with the following main-component contents: 100 mol.% Ln_2Se_3 (Ln = Sm, Gd, Tb, Yb), 98 mol.% Nd_2Se_3 [21,22].

For the preparation of 3 g $EuLnAgSe_3$ samples (Ln = La, Nd, Sm, Gd, Tb, Yb), the Ln_2Se_3, EuSe, and $Ag_{1.9}Se$ powders were ground together in an agate mortar and placed in a graphite crucible inside a quartz ampoule, which was then evacuated and sealed. Using a high-frequency induction furnace, the crucible was heated to 1750 ± 20 K, held at 1600 ± 20 K for one hour, and finally annealed at 1270 ± 10 K for 240 h. Dense, partially fused sinters were obtained.

2.2 Methods

Powder diffraction data for $EuErAgSe_3$ for Rietveld analysis were collected at room temperature on a Haoyuan DX-2700BH powder diffractometer (Cu-Kα radiation) using the equipment of the Krasnoyarsk Shared Research Center of the Siberian Branch of the Russian Academy of Sciences. The step size in 2θ was 0.01°, and the counting time was 0.2 s per step. The structure of $EuHoAgS_3$ was used as the starting model for the Rietveld refinement, which was carried out using TOPAS 4.2 [23,24].

Differential thermal analysis (DTA) was performed on a SETARAM SETSYS Evolution analyzer equipped with a PtRh-6/30 thermocouple. Powdered samples weighing 100 mg were placed in a cone-shaped quartz ampoule with a volume of 0.1 mL, which was evacuated to 0.2 Pa and sealed. Heating was conducted at a rate of 10 K/min. DTA results were processed using the SETSOFT 2000 software [25]. The baseline enclosing the peak area was obtained by approximating the baseline segments before and after the peak. The diffuse shape of the peak, or the presence of several overlapping components, resulted in a rather low accuracy of the integrated heat effect determination: ±17%.

Visual thermal analysis (VTA) was carried out on a VTA-T setup [26,27]. Samples weighing 50 mg were placed in cylindrical molybdenum crucibles 5 mm in diameter and 10 mm in height, which have a recess at the end face for the sample and a BP 5/25 thermocouple. The setup was evacuated to 0.3 Pa and filled with argon to a pressure of 1.1 bar. The heating rate ranged from 100 to 250 K/min. The condition of the sample in the crucible was recorded with an MC-HD-5 video camera. The setup was calibrated against the melting points of Cu, Ni, Pd, Pt, and white sapphire. The calibration curve was constructed with an

approximation accuracy of 98%. The accuracy of temperature determination is 0.5% of the temperature value.

Reflectance spectra were recorded on a Shimadzu UV-2600 spectrophotometer (Kyoto, Japan) using a powdered sample [28]. The distribution of chemical elements and the quantitative composition in the near-surface layer of the samples at a depth of about 3 μm were determined on a Tescan Mira 3 scanning electron microscope equipped with an Oxford Instruments X-Max EDS attachment. EDS analysis was carried out at an accelerating voltage of 20 kV. Processing of the EDS data and mapping were performed using the Aztec software. The instrumental accuracy of the determination of major components (content >10 wt.%) by the EDS method is ~0.9 wt.%, which yields an absolute error of ±0.5 wt.% at an element content of ~50 wt.%. The detection limit of the method is ~0.1–0.3 wt.% [29].

Microhardness was measured on an HMV-G21DT microhardness tester by the Vickers method [30]. Indentations were made automatically at an indenter load of 98.07 mN. With the 40× objective used, the accuracy of the indentation area measurement is 0.09 μm.

Microstructural analysis (MSA) of polished sections of the samples from various stages of synthesis and after DTA was performed on a Zeiss Axio Vert.A1 MAT microscope using the AxioVision SE64 software [31]. After DTA, the ampoule was mechanically processed until the sample substance was exposed and then polished to a mirror finish.

The large language model DeepSeek-R1 was employed as an auxiliary analytical tool for the crystal-chemical prediction of the formation of cubic $EuLnAgSe_3$ phases [32].

3 Results and Discussion

3.1 Crystal Structure of $EuErAgSe_3$

Diffraction data for $EuErAgSe_3$ were collected in the 2θ range of 10–100°. All peaks were indexed by the cubic cell (space group *Fm*-3*m*, $AgBiS_2$ structure type [33]) with parameters a = 5.95322(14) Å, V = 210.987(15) Å^3 close to those of $EuHoAgS_3$ [8]. Therefore, this structure was taken as the starting model for Rietveld refinement, which was performed using TOPAS 4.2. The site of Eu/Ho/Ag ions was occupied by Eu/Er/Ag ions (Fig. 1a) with fixed occupancies of 1/3 each, according to the suggested chemical formula. However, conventional powder X-ray diffraction does not allow the occupancies to be refined reliably; therefore, they were kept fixed. Thus, the $Eu^{2+}/Er^{3+}/Ag^{+}$ ions in $EuErAgSe_3$ are statistically distributed in the cation sublattice and occupy the same positions as the $Eu^{2+}/Ho^{3+}/Ag^{+}$ cations in the β-modification of $EuHoAgS_3$ [8] (Fig. 1b). The refinements were stable and gave low R-factors: R_{wp} = 8.45%, R_p = 5.96%, χ^2 = 3.75, R_B = 1.53%. The atomic coordinates and the main bond lengths are listed in Table 1.

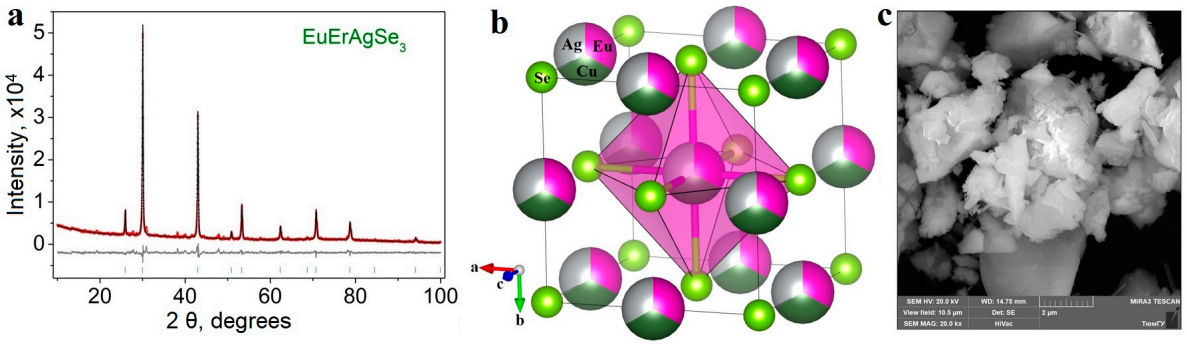

Figure 1: Rietveld difference plot (**a**), crystal structure (**b**), and image of particles (**c**) of the $EuErAgSe_3$ sample annealed at 1273 K.

The crystallographic data we obtained have been deposited at the Cambridge Crystallographic Data Centre and assigned the deposition number CSD-2466594. These data can be downloaded from the website—http://www.ccdc.cam.ac.uk/data_request/cif.

The $EuErAgSe_3$ powder obtained by grinding the annealed sample is dark brown in color. The phase particles exhibit faceting typical of substances crystallizing in the cubic system: angles of 60° and 90°, edges, and faces (Fig. 1c).

Table 1: Fractional atomic coordinates, isotropic displacement parameters ($Å^2$), and selected bond lengths (Å) for $EuErAgSe_3$.

Atom	*x*	*y*	*z*	B_{iso}	Occupancy	Bond	Distance
Eu	0.5	0.5	0.5	2.02(7)	1/3	Eu–Se^i	2.9700(1)
Er	0.5	0.5	0.5	2.02(7)	1/3	Er–Se^i	2.9700(1)
Ag	0.5	0.5	0.5	2.02(7)	1/3	Ag–Se^i	2.9700(1)
Se	0	0	0	1.35(7)	1	-	-

Symmetry code: (i) $x + 1/2, y + 1/2, z$.

3.2 Microstructure and Microhardness of the $EuErAgSe_3$

In the $EuErAgSe_3$ sample obtained by annealing at 1270 ± 10 K, SEM data reveal a uniform distribution of the chemical elements constituting the main phase. The elemental composition measured at points 1 and 2 (Fig. 2, Table 2) corresponds to stoichiometric $EuErAgSe_3$. The presence of individual grains of impurity phases was also detected; these were identified as Er_2O_2Se, $Er_2Si_2O_7$, $Ag_{2-x}Se$. The chemical composition of these phases indicates a tendency of erbium (III) selenide compounds to oxidize and form silicate compounds, which has also been noted in Refs. [18,34]. The involvement of erbium ions in side reactions leads to incomplete interaction between the components of the sample. The microhardness of the $EuErAgSe_3$ phase was measured on well-formed crystals, and at least 20 clear indentations were made. The median microhardness value is 340 ± 15 HV.

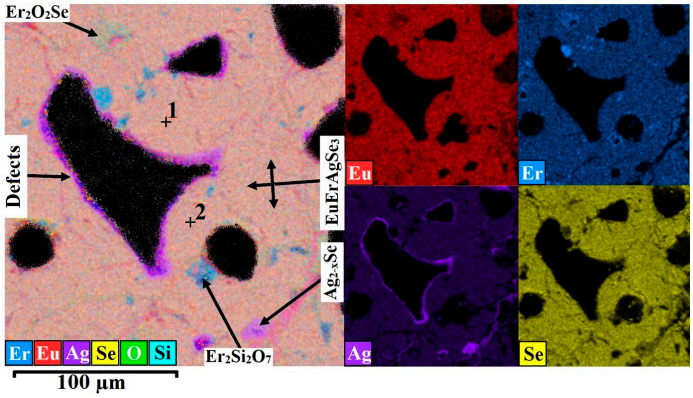

Figure 2: SEM image of the surface of a polished cross-section of the $EuErAgSe_3$ sample annealed at 1270 ± 10 K. Points 1 and 2 mark the spots where elemental analysis of the main phase was performed; the corresponding chemical composition is indicated in the figure.

Table 2: Content of chemical elements (at.%) at points 1, 2 (see Fig. 2) in a thin section of the $EuErAgSe_3$.

	Theor. (at.%)	Point 1 (at.%)	Point 2 (at.%)
Eu	16.6 (6)	18.1	18.3

Table 2: *Cont.*

	Theor. (at.%)	Point 1 (at.%)	Point 2 (at.%)
Er	16.6 (6)	15.1	15
Ag	16.6 (6)	21.5	19.6
Se	50	45.3	47.1
Compound	$EuErAgSe_3$	$Eu_{1.2}Er_{1.0}Ag_{1.4}Se_{3.0}$	$Eu_{1.2}Er_{1.0}Ag_{1.3}Se_{3.1}$

3.3 Optical Properties

The evaluation of the bandgap was conducted via the Tauc-like modified Kubelka-Munk treatment as described in [35]. Values $p = 1/2$ for dipole-allowed transitions occurring at a direct band gap, while $p = 2$ for dipole-allowed transitions near an indirect gap were used. $EuErAgSe_3$, as Fig. 3 illustrates, is featured by narrower bandgap in comparison with $EuErCuSe_3$: the bandgap for direct interband transition $E_{g\ direct} = 1.78 \pm 0.01$ eV (energy range for fitting 1.818–2.023 eV, Pearson R = 0.9989), and the bandgap for indirect transition $E_{g\ indirect} = 1.36 \pm 0.05$ eV (energy range for fitting 1.888–2.119 eV, Pearson R = 0.99889). The ion packing in the crystal structure of $EuErAgSe_3$ is less dense than for $EuErCuSe_3$. As XRD results show, for $EuErAgSe_3$ ($Eu_{1.33}Er_{1.33}Ag_{1.33}Se_4$) the cell volume per one formula unit is 210.99(1) $Å^3$. Ratio of the cell volume to the number of formula units equals to 141 $Å^3$ for $EuErCuSe_3$, while the unit cell volume of $EuErAgSe_3$ divided by 1.33 is equal to 157 $Å^3$, that indicates a denser packing in case of $EuErCuSe_3$. However, despite a denser packing in $EuErCuSe_3$, the Eu–Se distance is equal to 2.977 Å in $EuErAgSe_3$, while in $EuErCuSe_3$ it is equal to 3.066 Å.

Narrower bandgap of $EuErAgSe_3$ in comparison to $EuErCuSe_3$ correlates with the smaller Eu–Se distance, since at smaller Eu-Se distance a stronger crystal field at a separate Eu^{2+} ion must be expected. Stronger crystal field in case of a solitary Eu^{2+} ion in a lattice, as it is well-known, leads to a stronger red shift of a part of $5d$ energy levels of Eu^{2+}, which are responsible for the formation of the bottom of conduction band upon the formation of the band structure, and consequently, for the formation of fundamental absorption edge. Similar behavior of Eu^{2+} energy levels is demonstrated, e.g., in [36] where stronger crystal field results in the red shift of the absorption bands.

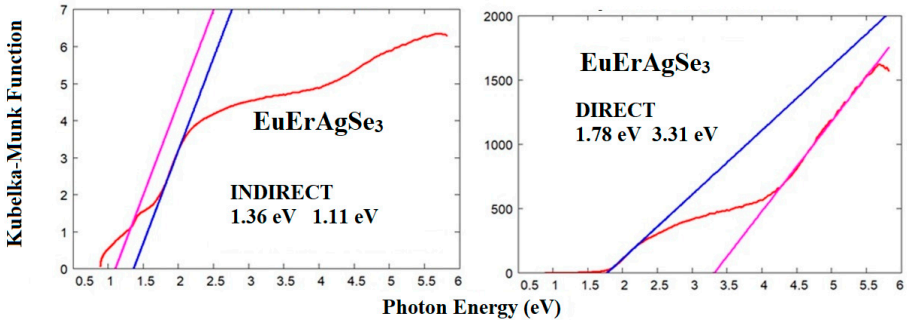

Figure 3: Kubelka-Munk Function for $EuErAgSe_3$ crystal modified for indirect (**left**) and for direct (**right**) interband transitions.

It is extremely interesting to note that Kubelka-Munk Function modified for indirect transition, aside from an evident region of the fundamental absorption onset, exhibits a minor step corresponding to 1.11 eV bandgap. Contrarily, for Kubelka-Munk Function modified for direct transition, aside from an evident region of the fundamental absorption onset, the higher lying linear region at 3.31 eV is pronounced. These features indicate onto a complicated band structure of $EuErAgSe_3$.

3.4 Thermal Properties

The diffraction characteristics of the $EuErAgSe_3$ phase did not noticeably change after the sample had been kept under ambient conditions for six months. During heating in the course of DTA, the $EuErAgSe_3$ phase begins to decompose. The DTA trace exhibits a peak at 798 K with a distinct linear portion in the endothermic temperature range of the sample (Fig. 4a). The enthalpy of the peak increases during thermal cycling and reaches its maximum value for the multi-phase sample obtained by annealing $EuErAgSe_3$ at 720 ± 10 K for 300 h. The peak is reproducible over heating and cooling cycles. The temperature closest to this peak is the decomposition temperature of the $EuSe_2$ phase, 842 K [16], however, the formation peak of $EuSe_2$ upon cooling is not detected by DTA.

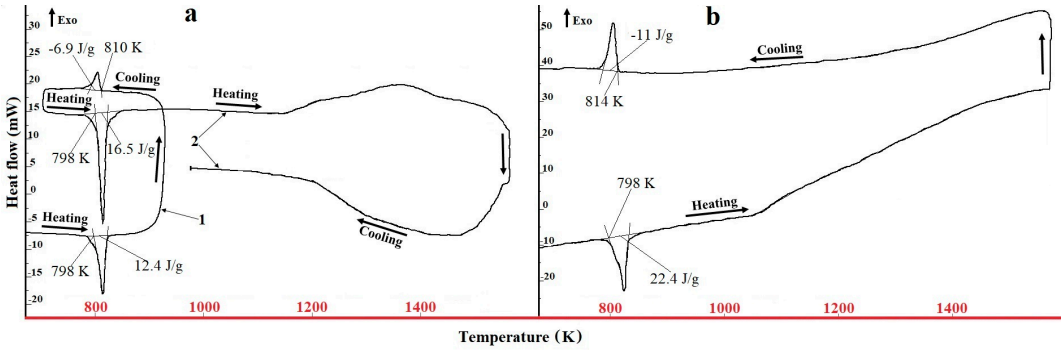

Figure 4: DTA curves of the high-temperature phase of $EuErAgSe_3$: 1 and 2—first and second heating–cooling cycles (**a**); DSC of the multiphase sample obtained by annealing $EuErAgSe_3$ at 720 ± 10 K (**b**).

The presence of a linear segment in the first half of the peak at 798 K indicates that the observed melting process corresponds to an invariant phase equilibrium on the phase diagram. It was established, by analogy with Cu_2S–EuS [37], that in the $Ag_{2-x}Se$–EuSe system a eutectic forms at 10 ± 1.5 mol% EuSe and 930 ± 10 K. Several samples of a possible ternary eutectic were studied; however, the recorded temperatures of the onset of heat absorption fell within the range 850–870 K.

Microstructural analysis was performed on approximately 15 mg of the molten (sweated) portion of the sample after DTA (Fig. 4a). On the polished section, $Ag_{2-x}Se$ grains form a continuous phase, in which very small amounts of at least three types of grains were identified. Fine needle-shaped crystals exhibited the same morphology as EuSe crystals in their eutectic with $Ag_{2-x}Se$. Small crystals forming chains were identified as Er_2Se_3. Several other crystals up to 2–3 μm in size remained unidentified. The grain morphology of the sample indicates the formation of a multicomponent eutectic. The peak at 798 K is caused by the melting of a eutectic situated close to the low-melting $Ag_{2-x}Se$ phase. The enthalpy of the peak at 798 K indirectly indicates the degree of decomposition of the $EuErAgSe_3$ phase during heating; this decomposition increases upon thermal cycling (Fig. 4a,b).

Anosov [38] links the formation of a phase that exists only at elevated temperatures with the appearance of an endothermic effect in the reaction of its synthesis from equilibrium phases. For instance, the formation of the high-temperature phase $CuSb_3Se_5$ is accompanied by a pronounced peak at 718 K, which increases the enthalpy of the phase by ΔH = 17.7 kJ/mol [39]. No peak corresponding to the heat effect of the formation of $EuErAgSe_3$ was detected by DTA. Prolonged annealing is required to achieve a high content of the $EuErAgSe_3$ phase in the samples. Most probably, $EuErAgSe_3$ is formed as a result of diffusion processes that start at temperatures of 1120–1170 K (Fig. 4a,b).

$EuErAgSe_3$ was heated in a Visual Thermal Analysis (VTA) setup from room temperature to 1270 ± 10 K at 250 K/min and subsequently to 1670 ± 30 K at 150 K/min; the sample remained polycrystalline throughout the process (Fig. 5a). After holding at this temperature for 5 min and cooling to ambient temperature within 4–5 min, the resulting product contained 95 mol.% $EuErAgSe_3$ with a = 5.9532 Å.

In a parallel experiment, a polycrystalline sample of $EuErAgSe_3$ was heated at the same rate to 1830 ± 30 K (Fig. 5b). A melt appeared in various parts of the sample, and intensive melting of the whole sample occurred. At 1970 ± 30 K, no crystals remained in the crucible, and the melt formed was transparent (Fig. 5c). According to XRD and microstructure examination, the phase samples that were rapidly heated to melting and crystallized from the melt predominantly contain the EuSe, $Ag_{2-x}Se$, Er_2O_2Se, and Er_2Se_3 phases, as well as up to several mol.% $EuErAgSe_3$. The phase compositions of the cooled samples and the transformation of $EuErAgSe_3$ into the melt indicate incongruent melting with the formation of a melt and crystals of the EuSe phase. The incongruent melting temperature of $EuErAgSe_3$ is estimated as 1830 ± 30 K.

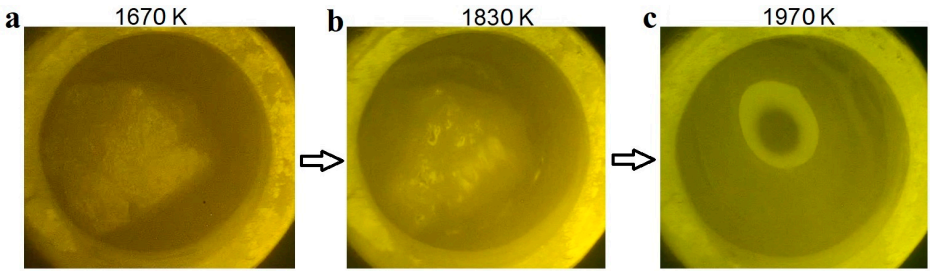

Figure 5: Appearance of the $EuErAgSe_3$ sample at the following temperatures: 1670 ± 30 K—polycrystalline state (**a**), 1830 ±30 K—bulk melting (**b**), 1970 ± 30 K—complete melt (**c**).

The formation of the $EuErAgSe_3$ phase at high temperatures (1120–1170 K) should be related to an increase in entropy due to the statistical distribution of three metal ions in the cation sublattice. The incongruent melting further confirms that at still higher temperatures (above 1830 K) the entropy contribution is no longer sufficient to stabilize the phase.

3.5 Prediction and Experimental Verification of the Formation of $EuLnAgSe_3$ Phases

The $EuErAgSe_3$ phase should be regarded as a chemical compound formed by isomorphic substitution in the EuSe phase of formal composition $(EuSe)_3$, where two Eu^{2+} cations are simultaneously replaced by Ag^+ and Er^{3+} cations. The formation of the phase is governed by several factors: size factor (ionic radii ratio), energetic factor (electronegativity ratio). The difference between the cation radius r(Eu^{2+}, CN = 6) = 1.17 Å and the average radius of the substituting cations r(Ag^+, CN = 6) = 1.15 Å and r(Er^{3+}, CN = 6) = 0.89 Å ($r_{av.}$ = 0.5(r(Ag^+) + r(Er^{3+})) = 1.02 Å) amounts to 12.8% [40]. According to the Hume-Rothery rules, the size factor (12.8%) does not exceed the threshold value of 15%, which makes substitution in the cation sublattice possible. The smaller $r_{av.}$ value accounts for the decrease in the unit cell parameters: EuSe a = 6.1676 Å, $EuErAgSe_3$ a = 5.95322(14) Å.

According to the Hume-Rothery rules for the formation of continuous solid solutions, the electronegativity difference Δχ must not exceed 0.4–0.5. In the system under consideration, the electronegativity differences are Δχ(Eu–Ag) = |1.2 − 1.93| = 0.73, Δχ(Ag–Er) = |1.93 − 1.24| = 0.67 [41,42]; these values noticeably exceed the indicated threshold. This precludes the formation of an extended solid solution between EuSe and $EuErAgSe_3$ and, on the contrary, promotes cation ordering and the formation of an individual compound. Application of the size and energy factors showed that $EuLnAgSe_3$ compounds should form for the entire rare-earth series except Sc. Literature data on $EuLnAgX_3$ phases and the proposed crite-

ria for the formation of $EuLnAgSe_3$ were communicated to the DeepSeek-R1 large language model [32], which also noted that "$EuLnAgSe_3$ compounds form for La–Lu, while the formation is more favorable for cerium-subgroup rare-earth elements".

Compositions with the ratio $Ag_{1.9}Se$:1.9EuSe:0.95Ln_2Se_3 (Ln = La, Nd, Sm, Gd) were synthesized. The samples containing the rare-earth elements La, Nd, and Sm exhibit a similar phase composition: EuSe, $Ag_{2-x}Se$ and also phases with the Th_3P_4 structure type, $EuLn_2Se_4$ (Ln = La, Nd, Sm) (Fig. 6). The sample with Gd contains 97 mol% $EuGdAgSe_3$, which crystallizes in the $AgBiS_2$ structure type with a = 5.9906(4) Å (Fig. 7a).

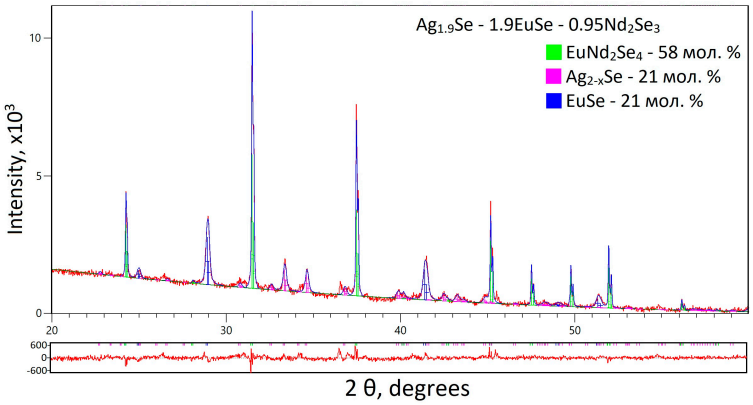

Figure 6: Difference X-ray diffraction pattern obtained by the Rietveld method for the sample with the initial phase ratio $Ag_{1.9}Se$:1.9EuSe:0.95Nd_2Se_3.

The phase composition data of the synthesized samples for La, Nd, Sm, Gd, and Er were analyzed using a language model. Based on these experimental results and several literature sources [6,7], the model proposed a new crystal-chemical factor (ρ). For ternary $AgLnSe_2$ selenides, the cubic $AgBiS_2$-type structure, which is a derivative of the NaCl-type, is stable only when the geometric criterion $\rho = r(Ln^{3+})/r(Ag^{+}) \leq 0.82$ is satisfied; this condition is met for Ln = Gd–Lu, Y. Exceeding this threshold ratio causes strong distortions of the octahedral polyhedron (see Section 3.1, Fig. 1b) that accommodates the cations, making it impossible to retain the cubic NaCl-type lattice. In the case of Cu-containing analogues, the $r(Ln^{3+})/r(Cu^{+})$ ratio even for the smallest rare-earth cation Lu^{3+} amounts to 0.861/0.77 ≈ 1.12, which significantly exceeds the indicated threshold. This explains why cubic $CuLnSe_2$ phases are unknown. The prompts will be provided in the Supplementary Materials.

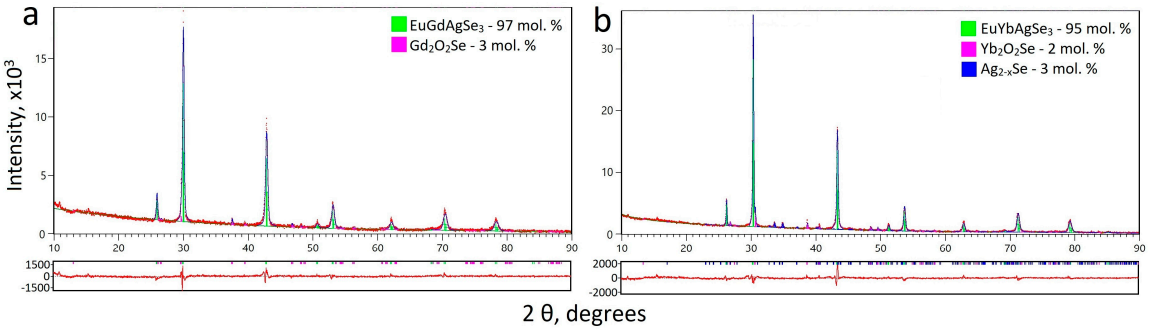

Figure 7: Difference X-ray diffraction pattern obtained by the Rietveld method for the sample $EuGdAgSe_3$ (**a**) and $EuYbAgSe_3$ (**b**).

The application of three criteria ($\Delta r \leq 15\%$, $\Delta\chi \geq 0.4$ and $\rho \leq 0.82$) to assess the formation of $EuLnAgSe_3$ phases showed that the cubic phase may appear exclusively for heavy rare-earth elements—Ln = Gd, Tb, Dy, Ho, Er, Tm, Yb, Lu, as well as for Y. For experimental verification of the above prediction, an additional $EuYbAgSe_3$ sample was synthesized; it contained 95 mol% $EuYbAgSe_3$ with a = 5.9312(5) Å and crystallized in the $AgBiS_2$ structure type (Fig. 7b). The decrease in the unit cell parameters in the $EuLnAgSe_3$ series is fully consistent with the lanthanide contraction along the series of Ln^{3+} ionic radii: Gd, Er, Yb (Fig. 8a). The SEM/EDS results for the $EuYbAgSe_3$ compound (Fig. 8b, Table 3) fully confirm the XRD data: the average elemental ratio for $EuYbAgSe_3$ over three spectra was 1.00 Eu:1.00 Yb:1.05 Ag:3.05 Se, which is in good agreement with the expected 1:1:1:3 stoichiometry.

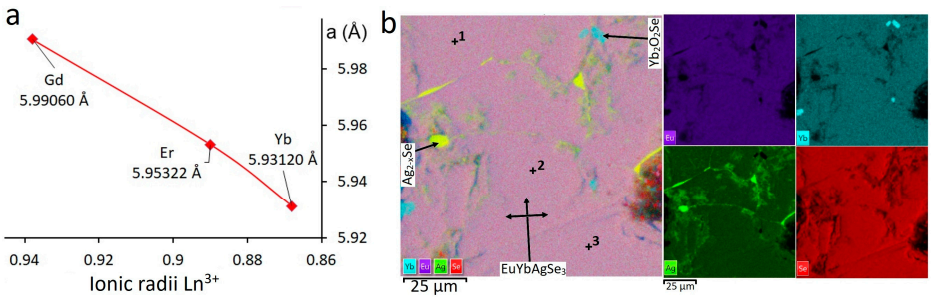

Figure 8: Plot of the unit cell parameters of $EuLnAgSe_3$ compounds (Ln = Gd, Er, Yb) as a function of the ionic radius of Ln^{3+} (CN = 6) (**a**); SEM image of the surface of a polished cross-section of the $EuYbAgSe_3$ sample annealed at 1270 ± 10 K, points 1–3 mark the spots where elemental analysis of the main phase was performed; the corresponding chemical composition is indicated in the figure (**b**).

Table 3: Content of chemical elements (at.%) at points 1–3 (see Fig. 8b) in a thin section of the $EuYbAgSe_3$.

Elements	Theoretical (at.%)	Point 1 (at.%)	Point 2 (at.%)	Point 3 (at.%)
Eu	16.6 (6)	16.4	16.5	16.1
Yb	16.6 (6)	16.9	16.7	16.6
Ag	16.6 (6)	17.7	17.1	17.1
Se	50	49.1	49.7	50.2
Compound	$EuYbAgSe_3$	$Eu_{1.0}Yb_{1.0}Ag_{1.1}Se_{3.0}$	$Eu_{1.0}Yb_{1.0}Ag_{1.0}Se_{3.0}$	$Eu_{1.0}Yb_{1.0}Ag_{1.1}Se_{3.1}$

The band gap of $EuGdAgSe_3$ was determined: an indirect transition at 1.42 eV and direct transitions at 1.72 and 4.05 eV (Fig. 9). The corresponding values for $EuErAgSe_3$ are 1.36 eV (indirect) and 1.78, 3.31 eV (direct). The decrease in the transition energies from Gd to Er is caused by the lanthanide contraction: the smaller ionic radius of Er^{3+} (0.890 Å vs. 0.938 Å for Gd^{3+}) leads to a reduction of the lattice parameter, which enhances the hybridization of Ln 5d and Se 4p states and, consequently, narrows the band gap.

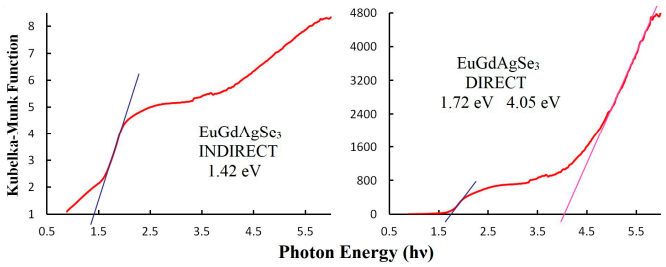

Figure 9: Kubelka-Munk Function for $EuGdAgSe_3$ crystal modified for indirect (left) and for direct (right) interband transitions.

All the experimental results fully confirm the proposed criteria for the formation of cubic $EuLnAgSe_3$ phases ($\Delta r \leq 15\%$ and $\rho \leq 0.82$ for Ag) and demonstrate the feasibility of the targeted prediction of new quaternary selenides with a cubic structure.

4 Conclusion

The $EuErAgSe_3$ phase was synthesized from samples of the EuSe and $AgErSe_2$ phases by annealing at 1270 ± 10 K and retains its structure upon cooling to ambient conditions. The $EuErAgSe_3$ crystallizes in the cubic system, space group *Fm*-3*m*, $AgBiS_2$ structure type, with a = 5.95322(14) Å. The $Eu^{2+}/Er^{3+}/Ag^{+}$ ions are statistically distributed over the cation sites. According to the Hume-Rothery rules, the formation of the phase became possible owing to a size factor of 12.8%, which lies below the 15% threshold. The considerable electronegativity differences, $\Delta\chi$(Eu–Ag) = 0.73 and $\Delta\chi$(Ag–Er) = 0.69, exceed the Hume-Rothery limit of 0.4–0.5 and account for the individuality of the $EuErAgSe_3$ phase, which does not form a solid solution with EuSe. The phase particles exhibit faceting, with angles of 60° and 90°. The direct optical band gap for direct transitions is 1.78 eV, and the indirect one is 1.36 eV. The $EuErAgSe_3$ phase begins to form at approximately 1120–1170 K, probably as a result of diffusion processes. The phase melts incongruently at a temperature of 1830 ± 30 K.

The possibility of the formation of $EuLnAgSe_3$ compounds (Ln = La–Lu) was predicted on the basis of geometric, energetic, and crystal-chemical factors. The decisive factor proved to be the crystal-chemical criterion: the cubic NaCl-type structure is stable only when the condition $\rho = r(Ln^{3+})/r(Ag^{+}) \leq 0.82$ is satisfied, which is met for Ln = Gd–Lu and Y. The phases $EuGdAgSe_3$ a = 5.9906(4) Å and $EuYbAgSe_3$ a = 5.9312(5) Å were synthesized. For $EuGdAgSe_3$, the band gap was determined: an indirect transition at 1.42 eV and direct transitions at 1.72 and 4.05 eV. Quantitative EDS analysis confirmed the stoichiometric elemental ratio in $EuYbAgSe_3$. The unit cell parameters vary linearly along the $EuLnAgSe_3$ series (Ln = Gd, Er, Yb). No quaternary compound forms for cerium-subgroup rare-earth elements.

The approach employing several types of criteria to predict the formation of cubic $EuLnAgSe_3$ phases can be effective in the search for new quaternary selenides with a cubic structure. The $EuLnAgSe_3$ phases are of potential interest owing to the presence of three cations statistically distributed over the cation sublattice.

Acknowledgement: This work was partially performed using resources of the Research Resource Center "Natural Resource Management and Physico-Chemical Research" (University of Tyumen).

Funding Statement: State Assignment No. FEWZ-2024-0052 for University of Tyumen from the Ministry of Science and Higher Education of the Russian Federation funded the large language model (LLM)-based phase prediction employed in this study.

Author Contributions: Conceptualization, Oleg Andreev, Navruzbek Habibullayev; methodology, Oleg Andreev, Navruzbek Habibullayev; investigation, Navruzbek Habibullayev, Ilya Yurev, Maxim Molokeev, Aleksandr Aleksandrovsky, Nikita Shulaev, Svetlana Volkova; data curation, Navruzbek Habibullayev; writing—original draft preparation, Oleg Andreev, Navruzbek Habibullayev, Maxim Molokeev, Aleksandr Aleksandrovsky; writing—review and editing, Olga Trofimova; visualization, Navruzbek Habibullayev, Maxim Molokeev, Aleksandr Aleksandrovsky; supervision, Oleg Andreev. All authors reviewed and approved the final version of the manuscript.

Availability of Data and Materials: Data available on request from the authors.

Ethics Approval: Not applicable.

Conflicts of Interest: The authors declare no conflicts of interest.

Supplementary Materials: The supplementary material is available online at https://www.techscience.com/doi/10.32604/cl.2026.085815/s1.

References

1. Pal K, Xia Y, Shen J, He J, Luo Y, Kanatzidis MG, et al. Accelerated discovery of a large family of quaternary chalcogenides with very low lattice thermal conductivity. npj Comput Mater. 2021;7:82. [CrossRef].
2. Ishtiyak M, Jana S, Karthikeyan R, Ramesh M, Tripathy B, Malladi SK, et al. Syntheses of five new layered quaternary chalcogenides $SrScCuSe_3$, $SrScCuTe_3$, $BaScCuSe_3$, $BaScCuTe_3$, and $BaScAgTe_3$: crystal structures, thermoelectric properties, and electronic structures. Inorg Chem Front. 2021;8(17):4086–101. [CrossRef].
3. Shahid O, Ray AK, Yadav S, Deepa M, Niranjan MK, Prakash J. Structure-property relationships and DFT studies of three quaternary chalcogenides: $BaCeCuSe_3$, $BaCeAgS_3$, and $BaCeAgSe_3$. Mater Res Bull. 2023;168:112469. [CrossRef].
4. Ruseikina AV, Baranov DN, Ostapchuk EA, Matigorov AV, Kasseinov RZ, Volkova SS, et al. Structural evolution and photovoltaic band gaps in the $EuREAgS_3$ series (RE = Tb, Dy, Ho, Tm, Yb). Inorg Chem Commun. 2026;186:116140. [CrossRef].
5. Liu Z, Li K, Sun Y, Wang RX. Upconversion photoluminescence and optical temperature sensing properties of $PbNb_2O_6$: Yb^{3+}, Ln^{3+} (Ln^{3+} = Er^{3+}/Ho^{3+}) ceramics. Chalcogenide Lett. 2024;21(12):977–88. [CrossRef].
6. Flahaut J. Sulfides, selenides and tellurides. Handb Phys Chem Rare Earths. 1979;4:1–88. [CrossRef].
7. Atuchin VV, Piskach LV, Parasyuk OV. Acentric phase formation in $AgLnX_2$ (Ln = Dy, Ho, Er; X = S, Se, Te) compounds. In: Proceedings of the 2010 IEEE 2nd Russia School and Seminar on Fundamental Problems of Micro/Nanosystems Technologis (MNST); 2010 Dec 9–11; Novosibirsk, Russia. p. 3–6. [CrossRef].
8. Ruseikina AV, Kol'tsov SI, Andreev OV, Pimneva LA. Crystal structure of $EuLnAgS_3$ (ln = Gd and Ho) compounds. Russ J Inorg Chem. 2017;62(12):1632–7. [CrossRef].
9. Sinha SP. Gadolinium break, tetrad and double-double effects were here, what next? Helvetica Chimica Acta. 1975;58(7):1978–83.[CrossRef].
10. Akagi T. Rare earth element tetrad effect. In: Geochemistry; encyclopedia of earth science. Dordrecht, The Netherlands: Kluwer Academic Publishers; 1998. p. 543–4. [CrossRef].
11. McLennan SM. Rare earth element geochemistry and the "tetrad" effect. Geochim Cosmochim Acta. 1994;58(9):2025–33. [CrossRef].
12. Jin M, Liang J, Qiu P, Huang H, Yue Z, Zhou L, et al. Investigation on low-temperature thermoelectric properties of Ag_2Se polycrystal fabricated by using zone-melting method. J Phys Chem Lett. 2021;12(34):8246–55. [CrossRef].
13. Karakaya I, Thompson WT. The Ag-Se (silver-selenium) system. Bull Alloy Phase Diagr. 1990;11(3):266–71. [CrossRef].
14. Ruseikina AV, Galenko EO, Soloviev LA, Zhernovnikova AM. Physicochemical analysis of the $2SrS{:}1Ln_2S_3{:}1Ag_{2-x}S$ (Ln = La, Nd, Dy, Er, Lu) compounds. Tyumen State Univ Herald. 2013;(5):49–57.
15. Reed TB, Fahey RE, Strauss AJ. Sealed crucible technique for thermal analysis of volatile compounds up to 2500°C: melting points of EuO, EuS, EuSe and EuTe. J Cryst Growth. 1972;15(3):174–8. [CrossRef].
16. Aitken JA, Cowen JA, Kanatzidis MG. Metamagnetic transition in $EuSe_2$: a new, metastable binary rare-earth polychalcogenide. Chem Mater. 1998;10(12):3928–35. [CrossRef].
17. Mizutani U. The Hume-Rothery rules for structurallly complex alloy phases. In: Book series on complex metallic alloys. Tokyo, Japan: World Scientific; 2010. p. 323–99. [CrossRef].
18. Andreev O, Atuchin V, Aleksandrovsky A, Denisenko Y, Zakharov B, Tyutyunnik A, et al. Synthesis, structure, and properties of $EuLnCuSe_3$ (ln = Nd, Sm, Gd, Er). Crystals. 2022;12(1):17. [CrossRef].
19. Reed TB, Fahey RE. Growth of EuO, EuS, EuSe and EuTe single crystals. J Cryst Growth. 1971;8(4):337–40. [CrossRef].
20. Yu J, Yun H. Reinvestigation of the low-temperature form of Ag_2Se (naumannite) based on single-crystal data. Acta Cryst E. 2011;67(9):i45. [CrossRef].
21. Folchnandt M, Schleid T. Single crystals of C-La_2Se_3, C-Pr_2Se_3, and C-Gd_2Se_3 with cation-deficient Th_3P_4-type structure. Z Anorg Allg Chem. 2001;627(7):1411–3. [CrossRef].

22. Fang CM, Meetsma A, Wiegers GA. Crystal structure of erbium sesquiselenide, Er_2Se_3. J Alloys Compd. 1995:273–5. [CrossRef].
23. Bruker AXS. TOPAS V4: General profile and structure analysis software for powder diffraction data—user's manual. Karlsruhe, Germany: Bruker AXS; 2008.
24. Pet'kov VI, Lavrenov DA, Asabina EA. Synthesis, structure, and thermal expansion of $BiCr_2(PO_4)_3$, $SbCr_2(PO_4)_3$, and $Bi_{1-x}SbxCr_2(PO_4)_3$ solid solution. Russ J Gen Chem. 2023;93(3):586–92. [CrossRef].
25. Shtykova MA, Vorob'eva VP, Fedorov PP, Molokeev MS, Aleksandrovsky AS, Elyshev AV, et al. Features of phase equilibria and properties of phases in the Sb-Sm-Se system. J Solid State Chem. 2022;316:123573. [CrossRef].
26. Yurev IO, Aleksandrovsky AS, Kamaev DN, Polkovnikov AA, Grigorchenko VM, Yarovenko AA, et al. The Sm_2S_3-X-SmS-Sm_2O_2S refractory system: thermal analysis, phase diagram, and properties of the phases. J Therm Anal Calorim. 2024;149(5):2057–73. [CrossRef].
27. Grigorchenko VM, Molokeev MS, Oreshonkov AS, Aleksandrovsky AS, Kertman AV, Abulkhaev MU, et al. Synthesis and properties of the NdSF compound, phase diagram of the NdF_3–Nd_2S_3 system. J Solid State Chem. 2024;333:124640. [CrossRef].
28. Shimadzu Corporation. Measurement of band gap of titanium (IV) oxide. [cited 2025 Jan 1]. Available from: https://www.shimadzu.com/an/sites/shimadzu.com.an/files/pim/pim_document_file/applications/application_note/13102/jpa113006.pdf.
29. Lavrent'ev YG, Karmanov NS, Usova LV. Electron probe microanalysis of minerals: microanalyzer or scanning electron microscope? Russ Geol Geophys. 2015;56(8):1154–61. [CrossRef].
30. Medeiros EE, Dias AMS. Experimental and numerical analysis of vickers hardness testing. Int J Res Rev Appl Sci. 2013;17:9–18.
31. Carl Zeiss Microscopy GmbH. Axio Vert.A1 operating manual. Jena, Germany: Carl Zeiss Microscopy GmbH; 2012.
32. Guo D, Yang D, Zhang H, Song J, Zhang R, Xu R, et al. DeepSeek-R1: incentivizing reasoning capability in LLMs via reinforcement learning. arXiv:2501.12948. 2025.
33. Geller S, Wernick JH. Ternary semiconducting compounds with sodium chloride-like structure: $AgSbSe_2$, $AgSbTe_2$, $AgBiS_2$, $AgBiSe_2$. Acta Cryst. 1959;12(1):46–54. [CrossRef].
34. Habibullayev NN, Naumov NG, Lavrov AN, Kuratieva NV, Aleksandrovsky AS, Oreshonkov AS, et al. Magnetic, optical, and thermic properties of $SrLnCuSe_3$ (ln = Dy, Ho, Er, Tm) compounds. Magnetochemistry. 2023;9(8):194. [CrossRef].
35. Landi S Jr, Segundo IR, Freitas E, Vasilevskiy M, Carneiro J, Tavares CJ. Use and misuse of the Kubelka-Munk function to obtain the band gap energy from diffuse reflectance measurements. Solid State Commun. 2022;341:114573. [CrossRef].
36. Aleksandrovsky AS, Malakhovskii AV, Zabluda VN, Zaitsev AI, Zamkov AV. Optical and magneto-optical spectra of europium-doped strontium tetraborate single crystals. J Phys Chem Solids. 2006;67(8):1908–12. [CrossRef].
37. Andreev OV, Ruseikina AV. Cu_2S–EuS phase diagram. Russ J Inorg Chem. 2012;57(11):1502–8. [CrossRef].
38. Anosov VY, Ozerova MI, Fialkov YY. Fundamentals of physicochemical analysis. Moscow, Russia: Nauka; 1976. 504 p.
39. Shtykova MA, Molokeev MS, Zakharov BA, Selezneva NV, Aleksandrovsky AS, Bubnova RS, et al. Structure and properties of phases in the $Cu_{2-x}Se$-Sb_2Se_3 system. The $Cu_{2-x}Se$-Sb_2Se_3 phase diagram. J Alloys Compd. 2022;906:164384. [CrossRef].
40. Shannon RD. Revised effective ionic radii and systematic studies of interatomic distances in halides and chalcogenides. Acta Cryst A. 1976;32(5):751–67. [CrossRef].
41. Lang PF. Revisiting electronegativity and electronegativity scales. J Chem Educ. 2025;102(1):424–9. [CrossRef].
42. Allred AL. Electronegativity values from thermochemical data. J Inorg Nucl Chem. 1961;17(3–4):215–21. [CrossRef].